Environmental TEM Investigation of Electrochemical Stability of Perovskite and Ruddlesden–Popper Type Manganite Oxygen Evolution Catalysts

*Daniel Mierwaldt, Vladimir Roddatis, Marcel Risch, Julius Scholz, Janis Geppert, Majid Ebrahimizadeh Abrishami, and Christian Jooss**

The sluggish kinetics of the oxygen evolution reaction (OER) is a grand challenge for energy storage technologies. Several perovskites and other oxides of earth-abundant elements are found to exhibit improved catalytic OER activity. However, less attention is paid to the electrochemical stability, an important factor for large-scale application. The ongoing search for stable catalysts calls for characterizing active catalyst surfaces and identifying mechanisms of deactivation, activation, or repair. In situ techniques are indispensable for these tasks. This study uses environmental transmission electron microscopy on the highly correlated perovskite $Pr_{1-x}Ca_xMnO_3$ and the Ruddlesden–Popper $Pr_{0.5}Ca_{1.5}MnO_4$ as model electrodes to elucidate the underlying mechanisms of the stability trends identified on rotating ring disk electrodes. An electron beam at fluxes well below those that would cause radiation damage is used to induce positive local electrode potentials due to secondary electron emission, driving electrochemical reactions in H_2O vapor. The stability of the model systems increases with increasing ionic character of the Mn—O bond, while more covalent bonds are prone to corrosion, which is triggered by formation of point defects in the oxygen sublattice.

1. Introduction

Electrochemical water splitting is a critical step of sustainable production of artificial fuels from renewable energies. Its efficiency is limited by large overpotentials of the anodic oxygen evolution reaction (OER).[1–7] Next to scarce noble metal oxides, several first-row transition metal oxides and, in particular, perovskite-based systems with the general formula ABO_3 perform well as OER catalysts.[6–10] Theoretical studies suggest that the catalytic activity of the four-electron transfer reaction forming molecular O_2 depends on strength and flexibility of

the bond between active site and reaction intermediates,[11,12] as well as on facile electron transfer.[13] In perovskites, bond strength and electron transfer are influenced by the transition metal valence, as well as by distance, angle, and hybridization of the metal–oxygen bonds. These parameters can be tuned by heterovalent A-site doping.[14,15] The required flexibility to adjust the surface acceptor states to the various reaction intermediates is facilitated by the capability of some transition metals to form different valence states.[12,16] Specifically, valence states of Mn-based OER catalysts are found to be between 3+ and 4+, as in the Mn_4Ca complex in natural photosynthesis.[4,17–22]

Searching for correlations between bond parameters and OER activity of perovskites, Suntivich et al. observed a volcano-like relationship between OER activity and bulk occupation of the σ-antibonding e_g states.[23] However, active surfaces can differ significantly from the equilibrium bulk states of a catalyst, involving dynamic point defect formation and annihilation, as, e.g., observed in TiO_2 or predicted for Au nanoparticles.[24,25] Point defect dynamics such as vacancies and interstitial atoms also have a strong impact on reaction mechanisms and activity in perovskites.[26,27] Furthermore, the reversibility of such point defect dynamics governs catalyst stability. The importance of understanding active states is underlined by the finding that high intrinsic activity is often correlated with low thermodynamic stability leading to corrosion and therefore limited long-term usability.[28–31]

Two principal scenarios for active sites and underlying reaction mechanisms are discussed for perovskite oxides, namely redox active metal versus redox active lattice oxygen sites. In the case of active metal sites, theory suggests that all OER steps occur at single metal centers.[12] Such a mechanism is supported by recent experiments on $La_{0.6}Sr_{0.4}MnO_3$, where a correlation between OER activity and Mn surface concentration is observed.[32,33] On the other hand, it has been proposed that surface lattice oxygen can be involved in OER by protonation (OH) and vacancy formation (V_O), based on in situ experiments[26,34] and recent theoretical works.[29,35] Note that previous studies have also shown lattice oxygen involvement for several highly active rutile catalysts.[36–38] Theoretical and experimental works suggest that lattice oxygen involvement is provoked by strong hybridization of

D. Mierwaldt, Dr. V. Roddatis, Dr. M. Risch, J. Scholz,
J. Geppert, Dr. M. E. Abrishami, Prof. C. Jooss
Institut für Materialphysik
Georg-August-Universität Göttingen
Friedrich-Hund-Platz 1, 37077 Göttingen, Germany
E-mail: jooss@material.physik.uni-goettingen.de

The ORCID identification number(s) for the author(s) of this article can be found under https://doi.org/10.1002/adsu.201700109.

ADVANCED
SCIENCE NEWS

www.advancedsciencenews.com

ADVANCED
SUSTAINABLE
SYSTEMS

www.advsustainsys.com

the metal–oxygen bond, which can shift the redox activity from metal to lattice oxygen surface sites due to ligand hole formation.[7,28,34,39,40] Thus, an understanding of the underlying microscopic mechanisms, the nature of active sites, and catalyst stability is necessary to rationalize the search for active and stable catalysts.

Using in situ X-ray absorption near-edge spectroscopy (XANES) and environmental transmission electron microscopy (ETEM) on the perovskite $Pr_{1-x}Ca_xMnO_3$ ($x \geq 0.3$), which has strong hybridization between O 2p and Mn 3d states, we have found strong evidence for lattice oxygen involvement in OER.[26,34,41] This was concluded from the experimentally observed Mn reduction at the surface under strongly oxidizing conditions, which can be explained by the formation of V_O and surface protonation acting as electron donors to Mn. This scenario was proven by the observation of vacancy ordering, showing that redox activity of lattice oxygen can open up a corrosion channel.[41] V_O formation during OER is facilitated by increasing Ca concentration and was interpreted by an increasing contribution of O 2p holes at the upper valence band edge based on band structure calculations. A comparative study of the perovskite (P) manganite $Pr_{1-x}Ca_xMnO_3$ and the related Ruddlesden–Popper (RP) system $Pr_{1-x}Ca_{1+x}MnO_4$ at equal doping levels of $x_{Ca} = 0.5$, 0.75, and 1 shows much higher stability of the RP structure, which was interpreted by a reduced O 2p character of the acceptor states, i.e., lower covalence factor, measured by X-ray spectroscopy at the O K-edge.[21] Different OER mechanisms, employing either O or Mn as redox active sites, therefore seem to enable different possible corrosion pathways and thus lead to remarkable differences in the stability of Mn-based electrodes.

We here present an ETEM study on the interplay of point defect chemistry and corrosion pathways, combined with ex situ rotating ring disk electrochemistry (RRDE). We compare the electrochemical stability of the perovskite $Pr_{0.7}Ca_{0.3}MnO_3$ (P73-PCMO) and the Ca-rich, layered RP system $Pr_{0.5}Ca_{1.5}MnO_4$ (RP-PCMO) in H_2O vapor at a fixed pressure of 0.5 Pa. The chosen model systems are comprised of the same building blocks, namely MnO_6 octahedra, which provide the hybridized, redox active electronic states, and similar Mn valence.[42] The systems have been chosen because of strong differences in covalence.[21] Moreover, RP systems show a much higher oxygen mobility parallel to the layers compared to perovskites and its change of lattice parameter as a function of oxygen content is one order of magnitude smaller, leading to reduced vacancy induced strain.[43,44] Differences in both properties are presumably important for explaining the observed enhanced stability of the RP phase under reactive conditions compared to the P phase. The ETEM study is extended to non-OER conditions in O_2 and/or He. To verify the stabilizing effect of lower covalence, the perovskite $Pr_{0.9}Ca_{0.1}MnO_3$ (P91-PCMO) with lower covalence factor than P73-PCMO is included in the ETEM study.

2. Results

2.1. Ex Situ Characterization

2.1.1. Electrochemistry by RRDE

Catalytic properties of P73-PCMO and RP-PCMO for OER are investigated by means of RRDE. The powders are deposited onto glassy carbon to form disk electrodes. A systematic study of structural and electrochemical properties including further doping levels of the two systems has been published elsewhere.[21]

The oxygen evolution activity is demonstrated by cyclic voltammetry (CV) in Ar-saturated electrolyte (0.1 M KOH) of the disk electrode and using the Pt ring electrode for detecting evolved oxygen molecules at a constant potential of 0.4 V versus reversible hydrogen electrode (RHE) via the oxygen reduction reaction. Representative CV curves of disk and ring current densities in **Figure 1**a,b show a comparably higher activity of the RP-PCMO both in terms of overpotential to obtain a current density of 50 µA cm^{-2} and in terms of current density at a potential of 1.65 V versus RHE. We observe slightly lower Tafel slopes for the P73-PCMO electrode. The same observations are made in O_2-saturated electrolyte, as summarized in Table S1 (Supporting Information). Ring currents are not superimposed by corrosion or capacitance, and correspond solely to the reduction of evolved oxygen.[32] Therefore, the simultaneous increase, i.e., similar Tafel slopes, of disk and ring currents suggests that the observed onset in fact corresponds to OER and the absence of parasitic processes.[45]

To evaluate the electrochemical stability of P73-PCMO and RP-PCMO, we compare the changes of consecutive voltage cycles relative to the 2nd cycle at a potential of 1.65 V versus RHE. These relative changes are presented in Figure 1c, showing significantly higher stability of the RP-PCMO. Note that the intermediate potential range is chosen to avoid contribution of capacitive effects at low potential and bubble formation at high potentials.

2.1.2. Covalence Analysis by XAS

X-ray absorption spectroscopy (XAS) at the O K-edge is very sensitive to the character of the ionocovalent Mn−O bond. As described in the Supporting Information, differences of the bond covalence can be qualitatively extracted from intensity differences of the low energy feature, reflecting the presence of O 2p hole states due to hybridization with the Mn 3d states.[21,46,47] X-ray absorption edges (total electron yield) of different P-PCMO and RP-PCMO samples at various Pr/Ca ratios are presented in Figure S1 (Supporting Information). The obtained covalence factors are plotted against the corresponding nominal Mn valence in Figure 1d. To compare the results of thin films and sub-micrometer-sized particles, the factors are normalized by the respective values for P55-PCMO. Covalence is found to be highest in Ca-doped P-PCMO, decreasing toward $PrMnO_3$ below half doping. In comparison, covalence is significantly lower in RP-PCMO, showing strong decrease with increasing Pr/Ca-ratio also for Ca-rich compositions.

Therefore, ex situ experiments demonstrate the correlation of electrochemical stability with the ionocovalent character of the Mn−O bonds. However, understanding the mechanistic origin of corrosion pathways requires in situ studies, as presented in the following section.

2.2. ETEM Experiments

Microscopic investigation of the catalyst surfaces under reactive conditions is performed in an ETEM. Representative

**ADVANCED
SCIENCE NEWS**

www.advancedsciencenews.com

**ADVANCED
SUSTAINABLE
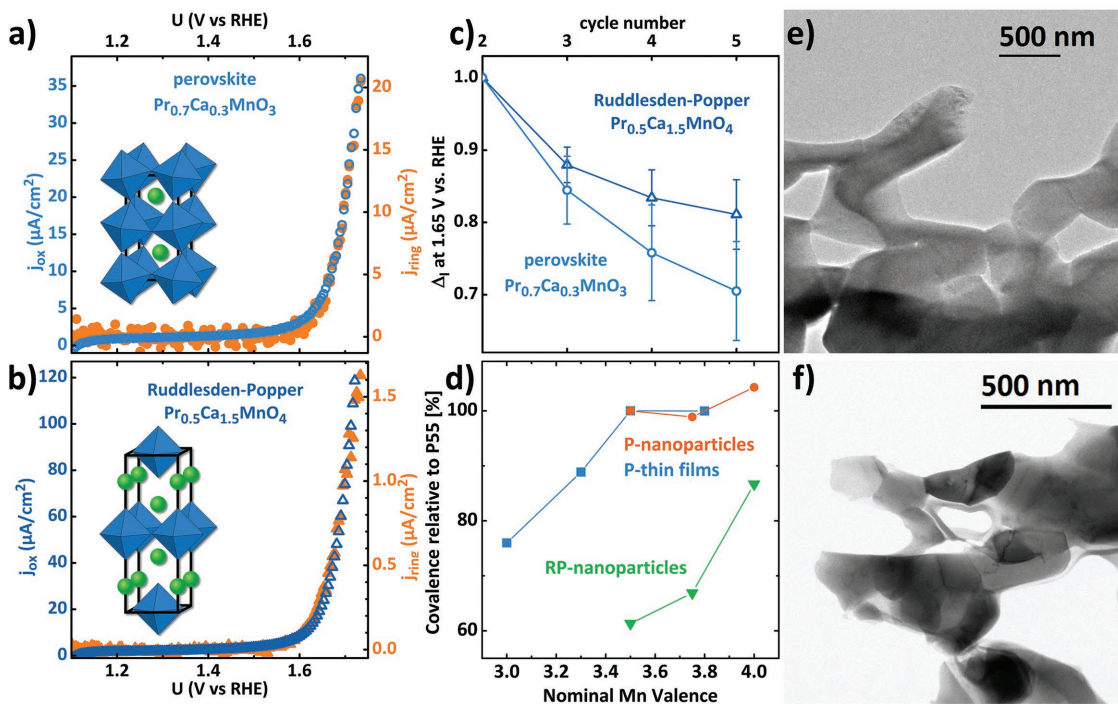SYSTEMS**

www.advsustainsys.com

Figure 1. a,b) Representative CV measurements (forward direction of the 5th scan) of powders of a) P73-PCMO and b) RP-PCMO are shown in blue and the corresponding ring currents in orange. The voltage is corrected for electrolyte resistance. Ring currents were obtained by CA at 0.4 V versus RHE. c) Relative changes of current density at 1.65 V versus RHE compared to the 2nd scan. All measurements were performed with 10 mV s^{-1} scan rate at 1600 rpm rotation in a,b) Ar-purged or c) O_2-purged 0.1 M KOH supporting electrolyte. d) Covalence of the Mn—O bond in $Pr_{1-x}Ca_xMnO_3$ perovskite (P) thin films (squares), P-particles (circles), and Ruddlesden–Popper (RP) particles (triangles). e,f) Low magnification brightfield TEM images of the ion milled e) P73-PCMO and f) RP-PCMO.

low magnification bright field TEM images of the ion milled specimen from sintered powder pellets are shown in Figure 1e (P73-PCMO) and Figure 1f (RP-PCMO). Crystal sizes of 80–800 nm are observed. We expose the catalysts to H_2O vapor at 0.5 Pa and to different pressures of O_2 or He. Unless specified otherwise, an electron beam of 4 nA and 100 nm diameter is used to stimulate and observe the specimen, corresponding to an electron flux density of about 32 000 e$^-$ Å^{-2} s^{-1}. At this rather high value, no structural changes due to beam damage are observed by high-resolution transmission electron microscopy (HRTEM) imaging in high vacuum and inert gas (He) during exposure for typically 50 min. Absence of oxygen knock-out from intact crystalline areas in high vacuum mode is proven by electron energy loss spectroscopy (EELS) analysis of Mn valence. In H_2O vapor, the electron flux has been found to be optimal in order to induce electrochemical activity.[48]

2.2.1. ETEM Analysis of P73-PCMO

The ETEM experiment presented in **Figure 2** demonstrates the beam driven formation of nanocrystals from the oxygen depleted amorphous surface and the underlying (001) facet of a P73-PCMO single crystal (orthorhombic *Pbnm* space group) in 0.5 Pa H_2O. The cross-section lamella is cut from an epitaxial thin film. An amorphous layer of 2–5 nm thickness due to ion milling and carbon contamination is observed on the pristine surface (Figure 2a). The contamination is being

removed upon exposure to the beam in vacuum of 10^{-4} Pa, while the ion beam damaged specimen material remains stable (Figure 2b; Video S1, Supporting Information). Exposure to the same electron beam in 0.5 Pa H_2O leads to rapid recrystallization of surface-near areas (Video S2, Supporting Information). The state of the specimen after 8 min of in situ recrystallization with ≈5 nm large crystallites on the surface is shown in Figure 2c.

Next, we present an ETEM experiment on a single crystalline (010) facet of a P73-PCMO particle. The pristine composition is confirmed by EELS and energy dispersive X-ray spectroscopy (EDX), as shown in the Supporting Information. **Figure 3**a shows a high-resolution image of the pristine surface and Video S3 (Supporting Information) demonstrates its stability under illumination by the electron beam in vacuum of 8 × 10^{-5} Pa. H_2O vapor is introduced and a pressure of 0.5 Pa is stabilized with blanked beam for about 45 min. Upon exposure to the beam under these conditions, nanocrystals of various orientations start to form at the particle surface (Figure 3b; Video S4, Supporting Information). Corresponding fast Fourier transforms (FFTs) of the indicated areas are shown in Figure 3c,d. The FFT of an exemplary area marked by the blue square is still clearly dominated by the original perovskite structure (Figure 3c), demonstrating that it is preserved in the bulk. The FFT of the surface crystal (Figure 3d) is consistent with the perovskite structure in new orientation with deviations from the pristine lattice parameters within 10 pm and also contains weak spots originating from the bulk.
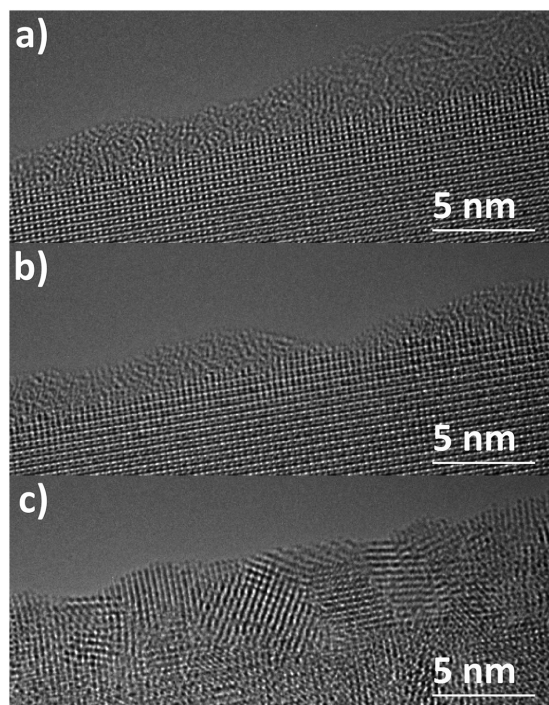
Figure 2. a) Epitaxial P73-PCMO thin film with amorphous surface layer due to specimen preparation by ion milling and carbon contamination. b) Remaining preparation induced layer, after slow removal of carbon contamination under electron beam illumination in high vacuum (10^{-4} Pa). c) In 0.5 Pa H_2O, ≈5 nm large crystallites start to form in random orientation on top of the single crystal surface.

Postmortem scanning transmission electron microscopy (STEM) and EELS analysis reveals that the experiment in H_2O ultimately leads to chemical decomposition of the P73-PCMO. In order to minimize further beam-induced reactions, postmortem analysis is performed after several hours of pumping the H_2O out of the microscope returning to a vacuum of ≈10^{-4} Pa. The high-angle annular dark field (HAADF) images of the reacted specimen in Figure 3e and Figure S2 (Supporting Information) show brightness variations between ≈5–10 nm large areas, resulting from variations in thickness and chemical composition. Since the scattering angle is limited to 100 mrad, the HAADF signal also contains some coherent contrast from different orientations of surface crystals. EEL spectra from areas A–D (Figure 3e) as well as from larger areas E–H (Figure S3, Supporting Information) show varying ratios of the contained cations, as summarized in **Table 1**. Details of the quantification procedure are given in the Supporting Information. Major loss of Mn is revealed in areas where the specimen has been illuminated under reactive conditions, as indicated by a strongly increased A-cation to Mn ratio compared to its stoichiometric value. Depletion of Mn increases with decreasing specimen thickness, indicating that surface reactions drive the perovskite nanocrystal formation as well as the subsequent decomposition of the perovskite into Pr-rich and Ca-rich phases. In areas G and H, which have not been exposed to the electron beam during the in situ experiment, almost no change in chemical composition is observed. In conclusion, P73-PCMO recrystallizes and subsequently decomposes whenever it is exposed to the combination of H_2O and electron beam at the chosen parameters.
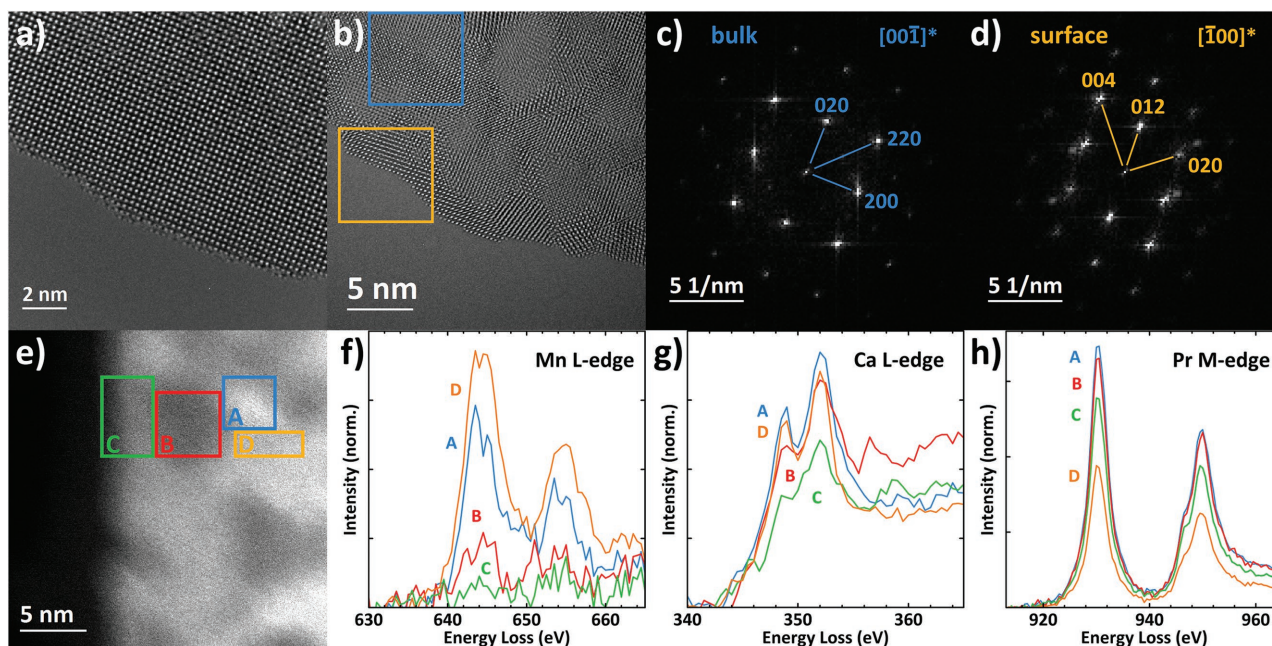
Figure 3. a) Pristine P73-PCMO (010) facet of a single crystal particle in ⟨001⟩ zone axis. b–d) Beam driven nucleation of misoriented perovskite nanocrystals at the surface, observed after 3 min of illumination in 0.5 Pa H_2O. c) FFTs show that the original crystal structure still dominates the bulk, d) while misoriented grains form at the surface. e) Postmortem HAADF-STEM shows brightness variations between 5 and 10 nm large areas, partly due to thickness variation as well as chemical decomposition. f–h) Postmortem EEL spectra of areas A–D marked in (e) at the Ca L-edge, Mn L-edge, and Pr M-edge demonstrate chemical decomposition due to structural disorder.

**ADVANCED
SCIENCE NEWS**

www.advancedsciencenews.com

**ADVANCED
SUSTAINABLE
SYSTEMS**

www.advsustainsys.com

Table 1. Postmortem EELS analysis of the P73-PCMO particle. Concentrations of Pr, Ca, and Mn atoms (in at%) are quantified by using the Pr M-edge, Ca L-edge, and Mn L-edge as described in the Supporting Information. Total relative thickness (t_{tot}/λ) has been calculated from simultaneously measured low loss spectra. It has been corrected for carbon contribution from surface contamination to give the specimen specific t/λ. HAADF images of the measured areas are shown in Figure 3e (areas A–D) and Figure S3 of the Supporting Information (areas E–H). Areas G and H were not illuminated by the electron beam during the in situ experiment and are close to the pristine composition.

Area	t/λ	Pr [at%]	Ca [at%]	Mn [at%]	(Pr + Ca)/Mn	Ca/(Pr + Ca)
Nominal composition		35.0	15.0	50.0	1.0	0.30
Pristine crystal		37.0	15.5	47.5	1.1	0.30
A	0.09	62.3	25.9	11.9	7.4	0.29
B	0.06	53.5	38.9	7.6	12.2	0.42
C	0.06	59.0	37.2	3.9	24.9	0.39
D	0.10	45.6	28.3	26.1	2.8	0.38
E	0.07	58.8	21.6	19.7	4.1	0.27
F	0.21	54.3	18.6	27.2	2.7	0.25
G (no beam)	0.37	36.5	12.4	51.1	1.0	0.25
H (no beam)	0.17	31.1	17.7	51.2	1.0	0.36

2.2.2. ETEM Analysis of P91-PCMO

A fundamentally higher stability of P91-PCMO compared to P-PCMO with higher Ca-content is observed in the ETEM under the same experimental conditions at 0.5 Pa H_2O. **Figure 4** shows the single crystalline (112) facet of a particle in ⟨110⟩ zone axis of the Pbnm structure during the experiment. The specimen keeps its single crystalline state over the entire course of the experiment, despite showing strong cationic dynamics in the uppermost atomic layer. As further discussed for experiments on RP-PCMO and in the Supporting Information, the very weak contrast of the light oxygen atoms confines our observations to movement of the cations.
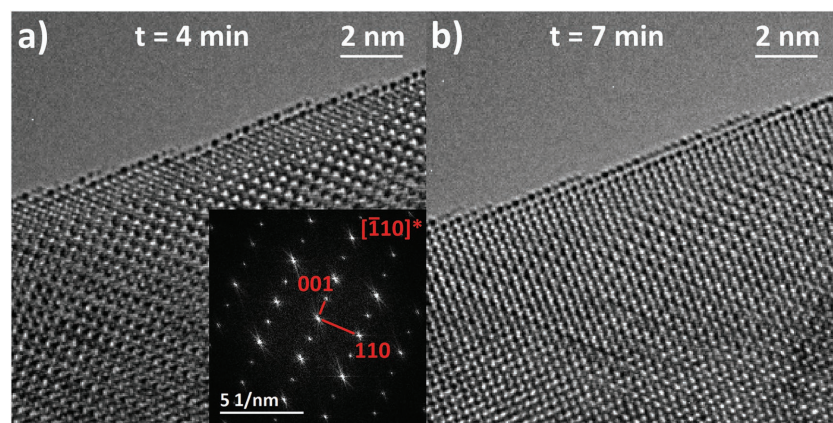
2.2.3. ETEM Analysis of RP-PCMO

RP-PCMO particles are exposed to H_2O vapor at 0.5 Pa. The example in **Figure 5** shows such a particle in ⟨110⟩ projection with a curved edge close to a (001) facet (orthorhombic *Fmm2* space group) with an amorphous surface layer due to lamella preparation. Upon exposure to the beam in H_2O, the up to 3 nm thick surface layer starts to crystallize mostly epitaxially on top of the Ruddlesden–Popper particle (Video S5, Supporting Information). Some amorphous material is still left on the surface after 7 min of illumination in H_2O (Figure 5a). Note that the area of the low indexed (001) surface facet (marked by arrows) acts as the most stable substrate leading to faster (and epitaxial) growth compared to edges, corners, and higher indexed surfaces. After 11 min, most of the surface material is crystallized and some misoriented grains start to grow (Figure 5b). After another 13 min, the misoriented grains have grown (Figure 5c). FFTs of the 550 nm^2 large areas at the observed surface after 7 and 24 min are shown in Figure 5d,e, respectively. The single crystal peaks of the RP-PCMO clearly dominate both FFTs, demonstrating its high structural stability. As can be seen in Video S5 (Supporting Information), the nanocrystals are mostly formed from the initially amorphous surface layer. This is in contrast to P73-PCMO, where nanocrystals are formed from bulk material.

2.2.4. EELS Analysis of RP-PCMO and P73-PCMO

A deeper understanding of the electrochemical processes underlying the different stability of RP-PCMO and P73-PCMO is gained from the study of changes in the Mn oxidation state via EELS. A RP-PCMO particle is investigated under the same conditions of 0.5 Pa of H_2O by means of in situ EELS at the O K-edge and Mn L-edge. (**Figure 6**a,b) HAADF-STEM images of the ≈20 × 40 nm^2 large areas are shown in Figure S4 (Supporting Information). The low energy feature of the O K-edge at around 529 eV represents excitation into hybridized antibonding states of Mn 3d e_g character.[42] It is therefore highly sensitive to changes in Mn valence state and hybridization of the Mn–O bond.[21,47] The shift of the onset toward lower energy demonstrates oxidation of the Mn during the in situ experiment. The postmortem valence is slightly lower, but still above the value of the pristine specimen. A similar shift of the edge onset to lower energy is found postmortem in a nearby area, which has not been illuminated while in contact with the H_2O. The Mn L-edge shows the same general trend with the highest valence state during the in situ experiment in H_2O vapor, as shown by the lowest intensity of the low energy flank of the L_3-edge at around 640 eV. The lowest valence is found in the initial state. The same edge shape is found postmortem in the area, which has not been illuminated during the experiment. Quantification of the Mn valence is given in Table S4 (Supporting Information). Details
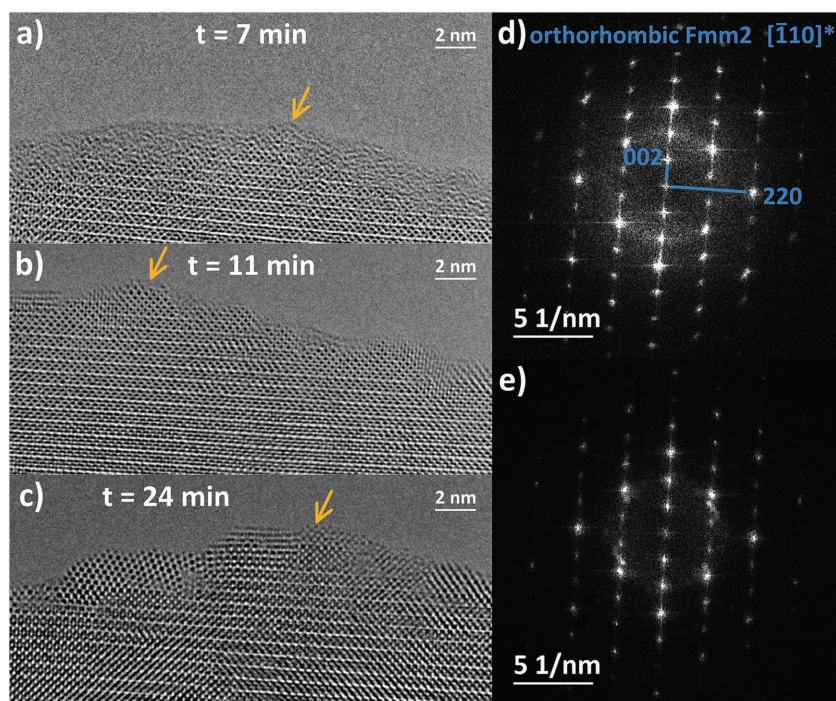

Figure 4. P91-PCMO single crystal observed at ⟨110⟩ zone axis after a) 4 min and b) 7 min of the ETEM experiment in 0.5 Pa H_2O. The FFT is shown as an inset.

Figure 5. a–c) RP-PCMO single crystalline particle with a near (001) facet observed in ⟨110⟩ zone axis after 7, 11, and 24 min of the in situ experiment in 0.5 Pa H_2O. The preparation induced amorphous surface layer (a) begins to crystallize epitaxially on top of the RP-PCMO (b). c) After more than 20 min, crystals of random orientation start to form at curved and higher indexed surfaces, while the epitaxy appears stronger on the flat (001) surface as marked by the arrow. d,e) FFTs of 550 nm^2 large areas after d) 7 and e) 24 min demonstrate the stability of the bulk structure during the entire time.

by a beam of 145 nm diameter and 1.2, 3.7, or 7.4 nA (flux densities of 4500–28 000 e^- $Å^{-2}$ s^{-1}). After 12 min at 1.2 nA in 0.5 Pa H_2O, some fcc nanocrystals are formed from the amorphous surface material, as demonstrated by the rotationally averaged FFT of a 16×16 nm^2 area at the edge (Figure S5, Supporting Information), while the Pbnm single crystal clearly dominates the FFT of a 32×32 nm^2 area (Figure S6a,b, Supporting Information). The reduced intensity of the low-energy feature of the O K-edge (528–530 eV) from the entire illuminated area of 16 500 nm^2 shows reduction of the P73-PCMO in comparison to an area that has not been illuminated during the ETEM experiment (Figure 6c). Higher beam current or H_2O pressure strongly accelerates the formation and growth of nanocrystals from the surface and bulk material, which is demonstrated by increasing number and intensity of polycrystalline peaks and decreasing intensity of the *Pbnm* single crystal peaks (Figure S6c–h, Supporting Information). As a result, the P73-PCMO increasingly decomposes into fcc nanocrystals (Figure S5, Supporting Information), which can lead to both oxidized or reduced Mn species (Figure 6c). In summary, we observe electronic changes of both the corroding P73-PCMO as well as the stable RP-PCMO.

on calibration and normalization of the spectra are presented in the Supporting Information.

Corrosion of P73-PCMO via nanocrystal formation and subsequent chemical decomposition is analyzed by postmortem EELS at the O K-edge after exposure to H_2O vapor at 0.5 or 5 Pa. The cross-section lamella, cut from an epitaxial thin film, is stimulated

2.2.5. ETEM Control Experiments on RP-PCMO in O_2 and/or He

Prior to the ETEM experiment presented in Figure 5, the same RP-PCMO particle has been exposed to the beam in vacuum and 0.7 Pa of He. Its amorphous surface layer is stable against beam damage in vacuum and is only partly being removed in
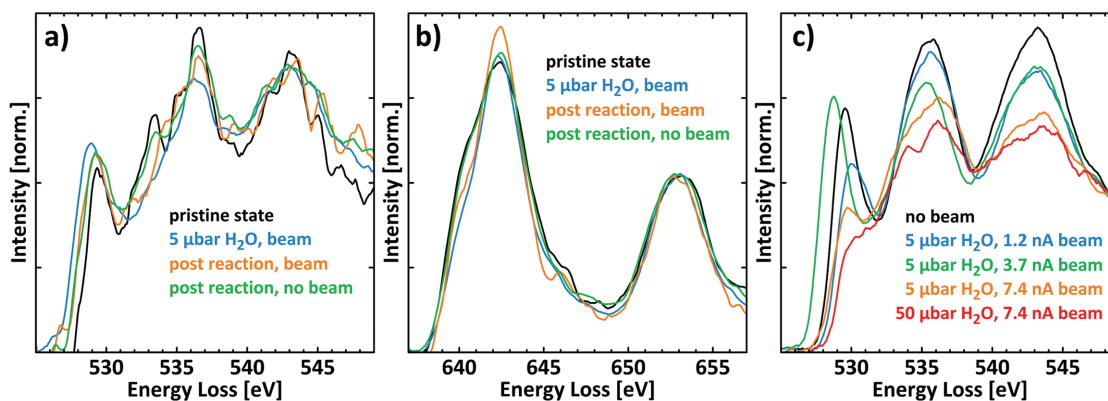

Figure 6. a,b) EELS at the Mn L-edge and O K-edge of a pristine single crystalline RP-PCMO particle observed in ⟨110⟩ zone axis (black), in 0.5 Pa H_2O (blue), and in high vacuum (HV) after the experiment of the same area (orange) and an area that had not been illuminated by the beam during the in situ experiment (green). c) Postmortem EELS at O K-edge of 5 areas of a P73-PCMO thin film after exposure to H_2O vapor. The areas were illuminated by 1.2 nA for 12 min (blue), 3.7 nA for 8 min (green), and 7.4 nA for 13 min (orange) in 0.5 Pa H_2O as well as by 7.4 nA for 8 min in 5 Pa H_2O (red). A spectrum from an unilluminated area is shown in black.
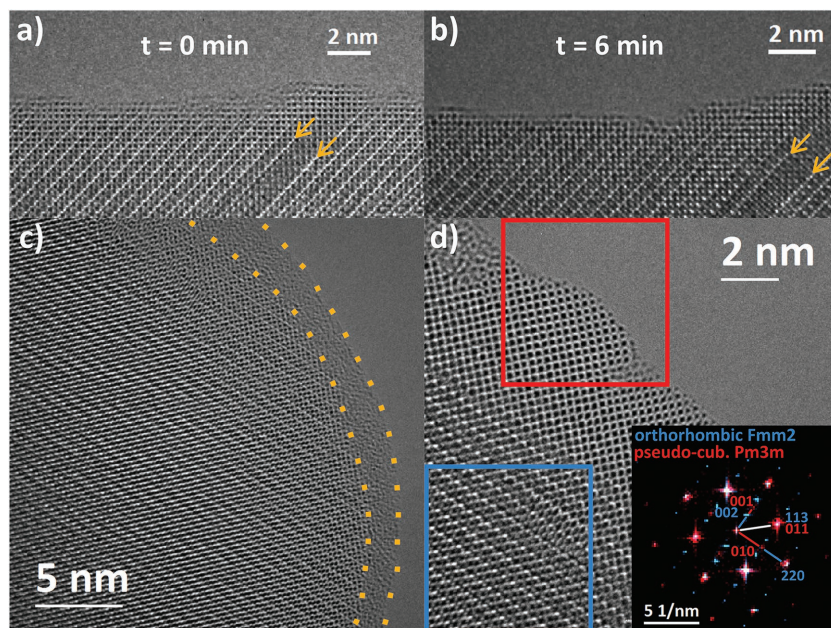
1700109 (6 of 10)

ADVANCED
SCIENCE NEWS
www.advancedsciencenews.com

ADVANCED
SUSTAINABLE
SYSTEMS
www.advsustainsys.com

Figure 7. a,b) RP-PCMO single crystal with a Pr-rich perovskite stacking-fault-like defect observed in ⟨110⟩ zone axis at different times of the in situ experiment in 100 Pa O_2. c,d) Other single crystal observed in ⟨110⟩ zone axis in 0.3 Pa O_2 + 0.3 Pa He. c) Pristine state with amorphous surface layer due to specimen preparation. d) Epitaxial crystallization in pseudocubic perovskite structure (⟨100⟩ zone axis) on top of the RP-PCMO single crystal during the in situ experiment, as demonstrated by the inset of corresponding FFTs.

He (Video S6, Supporting Information), presumably only some carbon-rich areas formed in high vacuum.

Other RP-PCMO particles are exposed to O_2 (or O_2 + He) to study the electrochemical oxidation of amorphous surface layers in the absence of catalysis. In the first experiment, we expose a particle to 100 Pa of O_2. The pristine state of a near (1-13) facet observed in ⟨110⟩ orientation of the *Fmm2* structure is shown in **Figure 7**a. Some stacking fault-like, Pr-rich defects of perovskite structure are observed due to incomplete reaction with CaO. Arrows mark such a layer of three perovskite unit cells. At this high oxygen pressure, in situ electron beam illumination results in strong cationic surface movement, especially at corners and curved facets (Video S7, Supporting Information). However, while some amorphous material is removed, it mostly crystallizes to form low indexed facets of the underlying single crystal (Figure 7b). Contrary to the trend with Ca-content in P-PCMO and despite the 200 times higher pressure compared to other ETEM experiments, the RP-PCMO is very stable during the 14 min of the in situ experiment.

The second experiment is performed on a crystal observed in ⟨110⟩ zone axis with a 3–4 nm thick layer of amorphous material on its surface due to lamella preparation (Figure 7c). The particle is exposed to a mixture (1:1) of He and O_2 at a pressure of 0.6 Pa. Under these conditions, the surface material crystallizes to form a Pr-rich perovskite, while the RP-PCMO acts as a stable substrate allowing epitaxial growth (Figure 7d). The epitaxial relationship is clearly demonstrated by FFTs of the orthorhombic bulk (blue, space group *Fmm2*) and the pseudocubic surface (red, space group *Pm3m*). Postmortem EELS points to depletion of Mn and Ca in the surface layer, due to

damage created during lamella preparation and leaching during the ETEM experiment (Figure S8, Supporting Information).

In summary, the ETEM experiments in Section 2.2 confirm the stability trends found by ex situ electrochemistry and provide valuable complementary insight: P91-PCMO and RP-PCMO retain their structure, while recrystallization of the P73-PCMO triggers and facilitates chemical decomposition.

3. Discussion

3.1. Electron Beam Driven Electrochemistry in ETEM

The comparison of stability trends in RRDE and ETEM studies as a function of material composition is a powerful approach for identifying destabilizing processes and corrosion channels. However, ETEM observations cannot be directly compared to ex situ electrochemical stability analysis due to differences in composition and conductivity of the electrolyte, pH value, pressure, and beam-induced effects.[34,41,48] Thus, distinguishing between electrochemical and beam damage effects is an important challenge of ETEM studies. Inelastic scattering of beam electrons has two main effects: First, the emission of secondary electrons creates a positive space charge within the material, which can drive electrochemical surface reactions. Second, knock-on damage induces point defects by displacing lattice atoms. Control experiments in high vacuum or He demonstrate that all systems, including P73-PCMO, are stable against beam damage, ruling out knock on processes as a significant mechanism for the observed effects during ETEM experiments. Additionally, instead of purely chemical effects, we observe beam-induced electrochemistry, which is supported by the fact that the structural and chemical effects as well as changes in oxidation state in reactive gasses (O_2, H_2O) only occur in combination with the electron beam, i.e., the observed changes set in only after unblanking of the beam. Macroscopic electrical measurements yield a specific resistance of the porous electrode materials of 4.7 kΩ cm. The investigated TEM specimens can therefore be estimated to have a ground resistance of roughly 500 MΩ. The surface potential under illumination by an electron beam of 4 nA is evaluated to a value of ≈0.7 ± 0.1 V by using equation (7) in Mildner et al.[41] The relatively large error in this order of magnitude estimation stems from uncertainties in estimated electric resistance of the porous thin lamella areas as well as from the deviation of the studied samples from planar lamella geometry underlying equation (7). Nevertheless, the estimated potential is electrochemically relevant for either driving material dependent electrode redox processes or even the OER. Increasing the electron flux accelerates the observed processes, but does not lead to new phenomena within the used limits.

**ADVANCED
SCIENCE NEWS**

www.advancedsciencenews.com

**ADVANCED
SUSTAINABLE
SYSTEMS**

www.advsustainsys.com

3.2. Corrosion Pathways and Driving Forces

We suggest that the observed stability trends can be mainly attributed to different character of the ionocovalent Mn—O bond. In the P-PCMO systems, Ca-doping shifts the O 2p and Mn 3d bands toward each other, increasing hybridization and covalence of the Mn—O bond, as shown by X-ray absorption spectroscopy (Figure 1d). Higher covalence shifts the O 2p band toward the Fermi level and thus facilitates the oxidation of surface lattice oxygen and the formation of point defects like V_O and protonation.[34,39] Redox active lattice oxygen can therefore participate in OER mechanisms, creating an active state that is vulnerable to corrosion.[35,49] Specifically, lattice oxygen mediated OER mechanisms bear the risk of V_O diffusion into the bulk of the catalyst, creating inhomogeneous strain.[50,51] This strain can drive nucleation of misoriented surface nanocrystals and therefore further drives the corrosion from an O depleted perovskite structure toward a chemically decomposed state, as observed in ETEM experiments on P73-PCMO (Figures 2 and 3). In previous ETEM and in situ XANES experiments in H_2O vapor under positive bias, surface reduction of P-PCMO at intermediate and high Ca doping was observed despite nominally oxidizing conditions due to formation of V_O acting as electron donors.[26,34,41] Phase decomposition of P-PCMO into A—O and Mn—O rich phases above a critical V_O concentration has also been observed for vacuum annealed thin films.[52]

By contrast, the increased ionic character of the Mn—O bond in Pr-rich P91-PCMO suppresses significant OER involvement of lattice O by preventing the formation of O^{1-} species and V_O.[53,54] Its remarkable stability in ETEM experiments suggests that no significant V_O formation occurs in contact with H_2O vapor at positive potentials (Figure 4). Accordingly, in situ XANES at the Mn L-edge of $PrMnO_3$ showed additional changes compared to Ca-doped specimens, which cannot simply be interpreted as Mn^{2+} formation.[26]

In summary, continuous V_O generation at the surface during OER and their migration into the subsurface can induce phase decomposition of the perovskite structure by inducing point defect strain. The highly strained grain boundaries between the formed nanocrystals may then further facilitate chemical decomposition. The subsequent beam-driven leaching of Ca and Mn or, in other words, knockout of light cations is shown by EELS (Figure 3e–h) In addition, the high solubility of Ca promotes the formation of weakly bound CaOH in the liquid surface layer, which is then likely to be knocked out by the beam. This can result in reduced or oxidized Mn species, as demonstrated in earlier ETEM experiments at different pressures of H_2O.[48]

However, the higher stability of RP-PCMO despite its much higher Ca content compared to P73-PCMO rules out Ca dissolution as the primary driving force for corrosion. Also, RP-PCMO shows clear Mn oxidation in 0.5 Pa H_2O, which points against the V_O formation of its perovskite counterparts and is probably caused by uptake of oxygen from H_2O molecules. The observed formation of nanocrystals in H_2O evolves from the amorphous surface material instead of recrystallization of the RP phase (Figure 5). Moreover, its ability to enforce epitaxial growth of the thick, initially amorphous surface layer during beam-driven crystallization in O_2+He further demonstrates its high structural stability (Figure 7d). However, crystallization forms Pr-rich P-PCMO instead of RP-PCMO, as the electron beam can knock Ca and Mn out of the weakly bound amorphous material. Leaching of the light cations apparently decreases the A/Mn ratio to nearly 1 (the stoichiometric value of P-PCMO). Furthermore, the A/Mn ratio could already have been decreased in the initial state of the amorphous TEM specimen regions due to preparation by ion milling.

In conclusion, we suggest that the more ionic character of the Mn—O bond of P91-PCMO and RP-PCMO (Figure 1d) inhibits excessive V_O formation, avoiding inhomogeneous strain at the catalyst surface. In addition, the rock salt-like AO double layers permit much easier relaxation of strain by nonstoichiometric oxygen compared to the perovskite structure.[44] Finally, increased diffusion within these layers may also play a role by homogenizing strain fields within the material.[55]

4. Conclusions

We demonstrate that all investigated systems (P73-PCMO, P91-PCMO, and RP-PCMO) are stable against beam damage in the TEM, unless their bond strength and phase stability are reduced by beam driven electrochemistry involving reactive gasses during ETEM experiments. In the case of P-PCMO, the electrochemical stability shows a strong dependence on Ca-doping, stemming from change of the Mn—O bond character. Most probably, the more ionic character in P91-PCMO stabilizes the material against point defect-driven corrosion, while P73-PCMO recrystallizes and chemically decomposes during ETEM experiments due to its highly covalent bond character. By contrast, RP-PCMO is much more stable despite its high Ca content, highlighting the importance of ionic bond character over effects of Ca-stoichiometry. These observations demonstrate that perovskite electrocatalysts of improved activity and stability can be developed systematically by tuning the defect chemistry by covalence of the transition metal–oxygen bonds.

5. Experimental Section

Sample Preparation: The perovskite powders were synthesized from calcium nitrate tetrahydrate $Ca(NO_3)_2$ $4H_2O$ (99%), manganese nitrate tetrahydrate $Mn(NO_3)_2$ $4H_2O$ (99.5%), praseodymium nitrate hexahydrate $Pr(NO_3)_3$ $6H_2O$ (99.9%), and gelatin using a wet chemistry method. Appropriate amounts of nitrates for 10 g of final product were dissolved in distilled water and stirred at room temperature for 20 min. Then, the 10 g gelatin solution, stirred at 40 °C for 30 min, was added to the solution of the cations and the whole solution was continually stirred at 60 °C for 2 h until it becomes clear with no precipitates or particulates. Then, a heat bath at 90 °C was used to evaporate the solvents until the desired resin-like product was obtained followed by drying at 200 °C for 5 min. Finally, the brownish black powder was calcined at 900 °C for 5 h.

Ruddlesden–Popper powders were prepared by conventional solid-state reaction but with a novel approach starting from a stoichiometric mixture of $Pr_{0.5}Ca_{0.5}MnO_3$ and CaO powders. The reagents were mixed in an agate mortar, ball-milled for 15 min, and heated in air at 1100 °C for 24 h. Structural analysis by X-ray diffraction and Rietveld refinement has already been published.[21]

The oxide electrodes for electrochemical measurements were prepared using a protocol published by Suntivich et al. but omitting Nafion.[56] The ink was prepared using acetylene black (AB) carbon

(99.9+%, Alfa Aesar) treated in nitric acid overnight at 80 °C and subsequently filtered and dried at 100 °C. Additionally, tetrahydrofuran (99.9+%, Sigma-Aldrich) and the respective oxide powder were mixed and sonicated for 30 min. The ink was composed of 1 mg mL^{-1} AB carbon and 5 mg mL^{-1} oxide particles. Finally, 2 × 5 µL of the ink was drop-casted on a freshly polished glassy carbon electrode (0.1257 cm^2 area, ALS Co. Ltd) to yield 0.4 mg$_{ox}$ cm$^{-2}_{disk}$ oxide loading, carefully controlling the drying to ensure a homogeneous coverage.

Particle TEM specimens were produced from pressed pellets of the respective powders. They were mechanically polished and ion-milled until perforation using a Gatan PIPS 691 system.

P73-PCMO thin films of 300 nm thickness were prepared by reactive ion beam sputtering (Xe sputter gas at 1 kV, 20 mA) from a sintered target onto single crystalline MgO substrate. TEM cross-section lamellae were cut by focused ion beam (30 kV, 7 nA–300 pA) and were subsequently thinned at 5 kV and 29 pA in a FEI Nova Nanolab 600 dual beam focused ion beam (FIB). Further thinning was done by Ar ion milling at 2 kV to 500 V in a Gatan 671 Precision Ion Polishing System. The final lamellae had an amorphous layer of 2–5 nm thickness on the single crystalline edge. Amorphization was accompanied by some oxygen depletion due to preferential etching as indicated by EELS based on a reduced Mn valence state, i.e., increased L_3/L_2 ratio and reduced intensity of the low-energy O K-edge feature.

RRDE Characterization: Electrochemical measurements were carried out with two Interface 1000E (Gamry Instruments Inc.) used as bipotentiostats assembled with a RRDE-3A rotator (ALS Co. Ltd) in a polytetrafluoroethylene (P73-PCMO) or glass (RP-PCMO) cell using a three-electrode configuration at room temperature. The measurements were performed in 0.1 M KOH prepared from 1 M stock solution (Sigma-Aldrich) and Milli-Q water (>16.5 MΩ cm) saturated with either O$_2$ or Ar (99.999%, Air liquid). The potentials were referenced to a saturated calomel electrode (ALS Co. Ltd) calibrated to the RHE scale by CV measurement of hydrogen evolution in H$_2$-saturated 0.1 M KOH, where the average voltages of zero current from the positive and negative-going CV scans were found at 0.997 V versus RHE. Additionally, the potentials were corrected for electrolyte resistance extracted from the high frequency intercept of the real impedance measured by impedance spectroscopy at the disk. Cleanliness of the Pt ring was checked before each experiment by matching CV with polycrystalline Pt.[57] CV measurements at the disk were performed at 10 mV s^{-1} and 1600 rpm. The ring voltage is always set to 0.4 V versus RHE, where the ring current is diffusion-limited. The currents of the oxide electrodes were corrected for the amount of the deposited oxide and corresponding surface area obtained by scanning electron microscopy (SEM) analysis of the particle size distribution.[21]

ETEM: The HRTEM images and related videos presented in this work were collected using an aberration-corrected, Schottky field-emission gun transmission electron microscope (FEI Titan 80-300 environmental (S)TEM) operated at 300 kV. The microscope base pressure under HV condition was below 10^{-4} Pa. During the experiments, up to 100 Pa of O$_2$, O$_2$+He, He, or H$_2$O vapor was introduced into the ETEM. The in situ videos were acquired using a script for Gatan's Digital Micrograph software. The script was provided by the Ernst Ruska-Centre (ER-C) for Microscopy and Spectroscopy. E-beam intensities indicated were measured using the e-beam current reading from the phosphor viewing screen. All particles or films were characterized in high vacuum before introducing any gas into the TEM chamber. At least three particles were tested and observed for each material to check the repeatability of observations.

EELS and EDX: Spectroscopy was performed in scanning diffraction mode, using a Gatan Quantum 965ER post-column energy filter for EELS and an Oxford Instruments X-Max 80 mm^2 silicon drift detector for EDX. Quantification of the EDX spectra on the basis of the Pr L-line, Ca K-line, and Mn K-line was performed by the Cliff Lorimer thin ratio section method using the commercial software INCA (Oxford Instruments). The energy resolution for EELS was ≈1 eV, measured as the full width at half height of the zero-loss peak. The convergence angle was 10.0 mrad and the effective collection angle was 21.9 mrad. Quantification of the EEL spectra was performed on the basis of the Pr M-edge, Ca L-edge, and Mn L-edge, which is described in more detail in the Supporting Information.

Supporting Information

Supporting Information is available from the Wiley Online Library or from the author.

Acknowledgements

Conflict of Interest

The authors declare no conflict of interest.

Keywords

[1] N. S. Lewis, D. G. Nocera, *Proc. Natl. Acad. Sci. USA* **2006**, *103*, 15729.

[2] N. Armaroli, V. Balzani, *Angew. Chem., Int. Ed.* **2007**, *46*, 52.

[3] A. Marshall, B. Børresen, G. Hagen, M. Tsypkin, R. Tunold, *Energy* **2007**, *32*, 431.

[4] H. Dau, C. Limberg, T. Reier, M. Risch, S. Roggan, P. Strasser, *ChemCatChem* **2010**, *2*, 724.

[5] R. Schlögl, *Top. Catal.* **2016**, *59*, 772.

[6] C. C. L. McCrory, S. H. Jung, J. C. Peters, T. F. Jaramillo, *J. Am. Chem. Soc.* **2013**, *135*, 16977.

[7] W. T. Hong, M. Risch, K. A. Stoerzinger, A. Grimaud, J. Suntivich, Y. Shao-Horn, *Energy Environ. Sci.* **2015**, *8*, 1404.

[8] Y. Matsumoto, E. Sato, *Mater. Chem. Phys.* **1986**, *14*, 397.

[9] R. A. Rincōn, E. Ventosa, F. Tietz, J. Masa, S. Seisel, V. Kuznetsov, W. Schuhmann, *ChemPhysChem* **2014**, *15*, 2810.

[10] M. S. Burke, S. Zou, L. J. Enman, J. E. Kellon, C. A. Gabor, E. Pledger, S. W. Boettcher, *J. Phys. Chem. Lett.* **2015**, *6*, 3737.

[11] J. Rossmeisl, Z.-W. Qu, H. Zhu, G.-J. Kroes, J. K. Norskov, *J. Electroanal. Chem.* **2007**, *607*, 83.

[12] I. C. Man, H. Y. Su, F. Calle-Vallejo, H. A. Hansen, J. I. Martínez, N. G. Inoglu, J. Kitchin, T. F. Jaramillo, J. K. Nørskov, J. Rossmeisl, *ChemCatChem* **2011**, *3*, 1159.

[13] S. Fletcher, *J. Solid State Electrochem.* **2009**, *13*, 537.

[14] J. O. Bockris, T. Otagawa, *J. Electrochem. Soc.* **1984**, *131*, 290.

[15] D. M. Sherman, *Am. Miner.* **1984**, *69*, 788.

[16] J. B. Goodenough, B. L. Cushing, in *Handbook of Fuel Cells*, Vol. 2, John Wiley & Sons, Ltd, Chichester, UK **2010**, pp. 1–14.

[17] I. Zaharieva, M. M. Najafpour, M. Wiechen, M. Haumann, P. Kurz, H. Dau, *Energy Environ. Sci.* **2011**, *4*, 2400.

[18] I. Zaharieva, P. Chernev, M. Risch, K. Klingan, M. Kohlhoff, A. Fischer, H. Dau, *Energy Environ. Sci.* **2012**, *5*, 7081.

[19] Y. Gorlin, B. Lassalle-Kaiser, J. D. Benck, S. Gul, S. M. Webb, V. K. Yachandra, J. Yano, T. F. Jaramillo, *J. Am. Chem. Soc.* **2013**, *135*, 8525.

[20] A. Ramírez, P. Hillebrand, D. Stellmach, M. M. May, P. Bogdanoff, S. Fiechter, *J. Phys. Chem. C* **2014**, *118*, 14073.

[21] M. Ebrahimizadeh Abrishami, M. Risch, J. Scholz, V. Roddatis, N. Osterthun, C. Jooss, *Materials* **2016**, *9*, 921.

[22] I. Zaharieva, D. González-Flores, B. Asfari, C. Pasquini, M. R. Mohammadi, K. Klingan, I. Zizak, S. Loos, P. Chernev, H. Dau, *Energy Environ. Sci.* **2016**, *9*, 2433.

[23] J. Suntivich, K. J. May, H. A. Gasteiger, J. B. Goodenough, Y. Shao-Horn, *Science* **2011**, *334*, 1383.

[24] Y.-G. Wang, D. Mei, V.-A. Glezakou, J. Li, R. Rousseau, *Nat. Commun.* **2015**, *6*, 6511.

[25] H. Zhao, F. Pan, Y. Li, *J. Mater.* **2017**, *3*, 17.

[26] D. Mierwaldt, S. Mildner, R. Arrigo, A. Knop-Gericke, E. Franke, A. Blumenstein, J. Hoffmann, C. Jooss, *Catalysts* **2014**, *4*, 129.

[27] J. T. Mefford, X. Rong, A. M. Abakumov, W. G. Hardin, S. Dai, A. M. Kolpak, K. P. Johnston, K. J. Stevenson, *Nat. Commun.* **2016**, *7*, 11053.

[28] K. J. May, C. E. Carlton, K. A. Stoerzinger, M. Risch, J. Suntivich, Y.-L. Lee, A. Grimaud, Y. Shao-Horn, *J. Phys. Chem. Lett.* **2012**, *3*, 3264.

[29] A. Grimaud, K. J. May, C. E. Carlton, Y.-L. Lee, M. Risch, W. T. Hong, J. Zhou, Y. Shao-Horn, *Nat. Commun.* **2013**, *4*, 2439.

[30] S. H. Chang, N. Danilovic, K.-C. Chang, R. Subbaraman, A. P. Paulikas, D. D. Fong, M. J. Highland, P. M. Baldo, V. R. Stamenkovic, J. W. Freeland, J. A. Eastman, N. M. Markovic, *Nat. Commun.* **2014**, *5*, 4191.

[31] B. Han, M. Risch, Y.-L. Lee, C. Ling, H. Jia, Y. Shao-Horn, *Phys. Chem. Chem. Phys.* **2015**, *17*, 22576.

[32] J. Scholz, M. Risch, K. A. Stoerzinger, G. Wartner, Y. Shao-Horn, C. Jooss, *J. Phys. Chem. C* **2016**, *120*, 27746.

[33] J. Scholz, M. Risch, G. Wartner, C. Luderer, V. Roddatis, C. Jooss, *Catalysts* **2017**, *7*, 139.

[34] S. Raabe, D. Mierwaldt, J. Ciston, M. Uijttewaal, H. Stein, J. Hoffmann, Y. Zhu, P. Blöchl, C. Jooss, *Adv. Funct. Mater.* **2012**, *22*, 3378.

[35] X. Rong, J. Parolin, A. M. Kolpak, *ACS Catal.* **2016**, *6*, 1153.

[36] M. Wohlfahrt-Mehrens, J. Heitbaum, *J. Electroanal. Chem. Interfacial Electrochem.* **1987**, *237*, 251.

[37] S. Fierro, T. Nagel, H. Baltruschat, C. Comninellis, *Electrochem. Commun.* **2007**, *9*, 1969.

[38] K. Macounova, M. Makarova, P. Krtil, *Electrochem. Commun.* **2009**, *11*, 1865.

[39] A. Grimaud, W. T. Hong, Y. Shao-Horn, J. M. Tarascon, *Nat. Mater.* **2016**, *15*, 121.

[40] C. Yang, A. Grimaud, *Catalysts* **2017**, *7*, 149.

[41] S. Mildner, M. Beleggia, D. Mierwaldt, T. W. Hansen, J. B. Wagner, S. Yazdi, T. Kasama, J. Ciston, Y. Zhu, C. Jooss, *J. Phys. Chem. C* **2015**, *119*, 5301.

[42] M. Sotoudeh, S. Rajpurohit, P. Blöchl, D. Mierwaldt, J. Norpoth, V. Roddatis, S. Mildner, B. Kressdorf, C. Ifland, C. Jooss, *Phys. Rev. B* **2017**, *95*, 235150.

[43] D. Lee, H. Lee, *Materials* **2017**, *10*, 368.

[44] T. Nakamura, Y. Ling, K. Amezawa, *J. Mater. Chem. A* **2015**, *3*, 10471.

[45] Q. Gao, C. Ranjan, Z. Pavlovic, R. Blume, R. Schlögl, *ACS Catal.* **2015**, *5*, 7265.

[46] F. M. F. de Groot, M. Grioni, J. C. Fuggle, J. Ghijsen, G. A. Sawatzky, H. Petersen, *Phys. Rev. B* **1989**, *40*, 5715.

[47] J. Suntivich, W. T. T. Hong, Y.-L. Lee, J. M. M. Rondinelli, W. Yang, J. B. B. Goodenough, B. Dabrowski, J. W. W. Freeland, Y. Shao-Horn, *J. Phys. Chem. C* **2014**, *118*, 1856.

[48] C. Jooss, S. Mildner, M. Beleggia, D. Mierwaldt, V. Roddatis, in *Controlled Atmosphere Transmission Electron Microscopy: Principles and Practice* (Eds: T. W. Hansen, J. B. Wagner), Springer International Publishing, Cham **2016**, pp. 301–329.

[49] W. G. Hardin, J. T. Mefford, D. A. Slanac, B. B. Patel, X. Wang, S. Dai, X. Zhao, R. S. Ruoff, K. P. Johnston, K. J. Stevenson, *Chem. Mater.* **2014**, *26*, 3368.

[50] U. Aschauer, R. Pfenninger, S. M. Selbach, T. Grande, N. A. Spaldin, *Phys. Rev. B: Condens. Matter Mater. Phys.* **2013**, *88*, 1.

[51] R. U. Chandrasena, W. Yang, Q. Lei, M. U. Delgado-Jaime, K. D. Wijesekara, M. Golalikhani, B. A. Davidson, E. Arenholz, K. Kobayashi, M. Kobata, F. M. F. de Groot, U. Aschauer, N. A. Spaldin, X. Xi, A. X. Gray, *Nano Lett.* **2017**, *17*, 794.

[52] T. Kramer, M. Scherff, D. Mierwaldt, J. Hoffmann, C. Jooss, *Appl. Phys. Lett.* **2017**, *110*, 243502.

[53] L. Rørmark, K. Wiik, S. Stølen, T. Grande, *J. Mater. Chem.* **2002**, *12*, 1058.

[54] E. I. Leonidova, A. A. Markov, M. V Patrakeev, I. A. Leonidov, V. L. Kozhevnikov, *Russ. J. Phys. Chem.* **2009**, *83*, 2009.

[55] A. Das, E. Xhafa, E. Nikolla, *Catal. Today* **2016**, *277*, 214.

[56] J. Suntivich, H. A. Gasteiger, N. Yabuuchi, Y. Shao-Horn, *J. Electrochem. Soc.* **2010**, *157*, B1263.

[57] P. Rheinländer, S. Henning, J. Herranz, H. A. Gasteiger, *ECS Trans.* **2013**, *50*, 2163.